Thermoelectric Properties and Microstructure of $Ba_8Al_{14}Si_{31}$ and $EuBa_7Al_{13}Si_{33}$

Cathie L. Condron,[†] Susan M. Kauzlarich,*[,†] Franck Gascoin,[‡,§] and G. Jeffery Snyder[‡]

Department of Chemistry, University of California Davis, One Shields Avenue, Davis, California 95616, and Materials Science, California Institute of Technology, 1200 East California Boulevard, Pasadena, California 91125

Received June 26, 2006. Revised Manuscript Received August 1, 2006

Powder samples of the type I clathrate phases, with the proposed stoichiometry $Ba_8Al_{16}Si_{30}$ and $Eu_2Ba_6Al_{16}Si_{30}$, were synthesized using direct reaction of stoichiometric amounts of the elements. Rietveld refinement of powder X-ray diffraction data is consistent with the clathrate type I structure. Composition, microstructure, and thermoelectric property measurements were made on hot-pressed pellets. Stoichiometry of the $Ba_8Al_{16}Si_{30}$ sample was determined from microprobe data to be $Ba_8Al_{14}Si_{31}$, close to the deficient framework solid solution of the general formula, $Ba_8Al_xSi_{42-3/4x}[]_{4-1/4x}$ ($x = 14$; [], open square indicates lattice defect). In the case of the rare-earth-substituted compound, microprobe analysis of the microstructure indicates that it is not single phase, but contains multiple components, most of the general clathrate stoichiometry. The majority phase has the stoichiometry $EuBa_7Al_{13}Si_{32}$. Both phases show conductivity typical of heavily doped semiconductors with negative Seebeck coefficients. The highest Seebeck coefficients are − 99 and −71 μV/K at 1192 K for $Ba_8Al_{14}Si_{31}$ and $EuBa_7Al_{13}Si_{33}$, respectively. The maximum zT is 0.34 at 1150 K and 0.22 at 1165 K for $Ba_8Al_{14}Si_{31}$ and $EuBa_7Al_{13}Si_{33}$, respectively.

Introduction

Thermoelectric devices have gained renewed interest for environmentally benign power generation.[1−3] If sufficiently efficient, thermoelectric devices can be developed to utilize waste heat sources, such as geothermal vents or automotive exhaust heat, to produce electrical power. Such power generation would require minimal amounts of fossil-energy consumption and would produce virtually no harmful emissions.

A good thermoelectric material requires a combination of high electrical conductivity (σ) or low electrical resistivity (ρ), low thermal conductivity (κ), and high thermopower or Seebeck coefficient (S), ultimately resulting in a high figure of merit ($zT = S^2T/\rho\kappa$, where T is temperature).[3] Materials that best meet these requirements are typically heavily doped, small band gap semiconductors or semimetals. Such materials provide a balance between the high Seebeck coefficient of semiconductors and the low electrical resistivity of metals.

In general, materials that contain light elements are often not considered for thermoelectric materials because heavy elements are normally associated with low lattice thermal conductivity. However, Si−Ge alloys,[4] transition-metal disilicides,[5−7] metal chalcogenides,[8,9] several boron compounds,[10,11] and the oxide material $TiO_{1.1}$[12] have attracted attention for high-temperature thermoelectric applications, where the lattice contribution is less important. A highly-crystalline material typically has lattice thermal conductivity decreasing with temperature as $1/T$ while the electronic contribution is flat or increasing with temperature because of the additional T term in the Wiedemann−Franz relation between electrical resistivity and electronic contribution to the thermal conductivity $\kappa_e = LT/\rho$ (where L is the Lorenz factor). For example, n-type SiGe has provided a surprisingly high figure of merit and remains a unique light element material for thermoelectric applications.[4]

Some ternary clathrate phases, which combine a small amount of heavy atoms within a light atom framework, show excellent thermoelectric figures of merit.[13−15] For example, $Ba_8Ga_{16}Ge_{30}$, grown using the Czochralski method, shows a zT of 1.35 at 900 K.[16] This promising figure of merit exemplifies the importance of exploring light element ternary

* To whom correspondence should be addressed. E-mail: smkauzlarich@ucdavis.edu.
[†] University of California Davis.
[‡] California Institute of Technology.
[§] Current address: Laboratoire de Physico-Chimie de la Matière Condensée, Université Montpellier 2, place Eugène Bataillon, 34095 Montpellier Cedex 5, France.

(1) Ma, X.; Riffat, S. B. *Appl. Therm. Eng.* **2003**, *23*, 913.
(2) Chen, G.; Dresselhaus, G.; Dresselhaus, M. S.; Fleurial, J. P.; Caillat, T. *Int. Mater. Rev.* **2003**, *48*, 45.
(3) Wood, C. *Rep. Prog. Phys.* **1988**, *51*, 459.
(4) Bhandari, C. M.; Rowe, D. M. *Thermal Conduction in Semiconductors*; Wiley Eastern Limited: New Delhi, India, 1988.
(5) Nishida, I. *Phys. Rev. B* **1973**, *7*, 2710.
(6) Nishida, I.; Sakata, T. *J. Phys. Chem. Solids* **1978**, *39*, 499.
(7) Kojima, T. *Phys. Status Solidi A* **1989**, *111*, 233.
(8) Bass, J. C.; Elsner, N. B. In *3rd International Conference on Thermoelectric Energy Conversion*; Rao, K. R., Ed.; IEEE: New York, 1980; p 8.
(9) Nakahara, J. F.; Takeshita, T.; Tschetter, M. J.; Beaudry, B. J.; Gschneidner Jr., K. A. *J. Appl. Phys.* **1988**, *63*, 2331.
(10) Wood, C.; Emin, D. *Phys. Rev. B* **1984**, *29*, 4582.
(11) Yugo, S.; Sato, T.; Kimura, T. *Phys. Lett.* **1985**, *46*, 842.
(12) Okinaka, N.; Akiyama, T. In *2005 International Conference on Thermoelectrics*; IEEE: New York, 2005; p 34.
(13) Cohn, J. L.; Nolas, G. S.; Fessatidis, V.; Metcalf, T. H.; Slack, G. A. *Phys. Rev. Lett.* **1999**, *82*, 779.
(14) Nolas, G. S. *Mater. Res. Soc. Symp. Proc.* **1999**, *545*, 435.
(15) Nolas, G. S.; Weakley, T. J. R.; Cohn, J. L.; Sharma, R. *Phys. Rev. B* **2000**, *61*, 3845.

10.1021/cm061483u CCC: $33.50
Published on Web 09/07/2006

clathrate phases. Although extensive work has been published on the Ga−Ge clathrates,[13−15] very little has been reported on the Ga−Si and Al−Si clathrate phases. Thermoelectric properties of $Ba_8Ga_8Si_{36}$, $Ba_8Ga_{16}Si_{30}$, and $Eu_2Ba_6Ga_8Si_{36}$ prepared by arc melting have been measured,[17−21] with an estimated zT of 0.87 at 870 K for $Ba_8Ga_{16}Si_{30}$.[19] $Ba_8Ga_{16}Si_{30}$ phases are reported to melt congruently, with a melting point between 1384 and 1470 K, depending on the stoichiometry.[19]

Similarly, very few Al−Si clathrates have been studied for thermoelectric properties and none measured at high temperature where zT is maximized. Thermoelectric properties of $Ba_8Al_{16}Si_{30}$, $Ba_8Al_{12}Si_{33}$, and $Sr_8Al_{10}Si_{36}$, and $Eu_2Ba_6Al_{16}Si_{30}$ prepared by arc melting and annealing, have been briefly investigated. Out of these, $Ba_8Al_{16}Si_{30}$ is the most promising, with a room-temperature Seebeck coefficient of approximately $-48\ \mu$V/K.[17,18] Recently, a new investigation of the Al−Si clathrate phases has taken place in hopes of optimizing stoichiometry, and thus thermoelectric properties.[22] The Al−Si clathrate phases are attractive candidates not only because they offer a light element alternative to the Ga−Ge phases but also because they are expected to exhibit higher melting points than the Ga−Ge phases, thereby expanding the temperature regime where these phases may be applicable.

In this paper, the high-temperature thermoelectric properties of two clathrate phases, $Ba_8Al_{14}Si_{31}$ and $EuBa_7Al_{13}Si_{33}$, prepared by reaction of the elements with ideal stoichiometries according to the phases $Ba_8Al_{16}Si_{30}$ and $Eu_2Ba_6Al_{16}Si_{30}$ and characterized by powder X-ray diffraction are presented. The samples were then hot-pressed, and the composition and microstructure were investigated via microprobe analysis. Measurements of electrical resistivity, thermal diffusivity, and the Seebeck coefficient in the temperature range 300−1200 K, the thermoelectric properties in the region of interest for such clathrates, have been measured and will be discussed.

Experimental Section

Sample Preparations. $Ba_8Al_{14}Si_{31}$ and $EuBa_7Al_{13}Si_{33}$ were synthesized by direct reaction of the elements according to the ideal stoichiometry for clathrate phases of $Ba_8Al_{16}Si_{30}$ and $Eu_2Ba_6Al_{16}Si_{30}$: Ba (Johnson Matthey, 99.9%), Eu (Ames Lab, 99.99%), Si (AESAR, 99.999%), and Al (Matheson Colemen and Bell 99.6%). Elements were loaded into alumina crucibles that were capped, placed in a fused silica tube, and sealed under 1/5 atm Ar. The reaction vessel was heated to 800 °C for 7 days. After 7 days, the furnace was turned off and allowed to cool to room temperature before reaction vessels were removed. The reaction product was ground and reheated several times to promote sample homogeneity. To obtain a dense sample, we hot-pressed finely ground powder in high-density graphite dies (POCO). The hot-pressing was conducted at a pressure of about 20000 psi and at 900 °C for 1 h under an argon atmosphere. A cylinder several mm long and 12 mm in diameter was thus obtained. The density of the pellet (calculated from measured dimensions and weight) was found to be about 99% of the theoretical density.

Characterization. X-ray powder diffraction data were collected with a Scintag PAD-V employing Cu Kα radiation. Data acquisition for both phases was performed with WinAcq software. Sample analyses and Rietveld refinement of selected samples were performed using the REITICA software package. The peak profile was chosen to be pseudo-Voigt (Howard asymmetry) and the background was fit to a fifth-order polynomial. Atomic positions, as well as the overall temperature factors, were held constant.

Microprobe analysis was performed on polished pressed pellets. The samples were placed in a Cameca SX100 electron microscope equipped with a wavelength-dispersive spectrometer. The microprobe was operated at a 15 nA beam current and 20 keV accelerating potential. Net elemental intensities for Al and Si were determined with respect to pure elemental calibration standards that were polished before the measurement to ensure the elements were not oxidized. $EuPO_4$ and $BaAl_{3.54}Si_{0.41}$ were used as standards to determine the net elemental intensities for Eu and Ba, respectively. Totals for all analyses were 100%. The elemental stoichiometries of the majority phases were quantitatively determined to be $Ba_{8(0.07)}Al_{14.0(0.4)}Si_{30.8(0.3)}$ and $Eu_{1.1(0.6)}Ba_{6.9(0.7)}Al_{12.8(0.3)}Si_{32.9(0.3)}$; standard deviations are given in parentheses.

A Netzsch Thermal Analysis STA 409 PC was used to evaluate the thermal properties of $Ba_8Al_{14}Si_{31}$ and $EuBa_7Al_{13}Si_{33}$ between 298 and 1373 K. After a baseline was established, pieces of the hot-pressed pellet (40−60 mg) were placed in alumina crucibles and heated under vacuum at 10 K/min with an acquisition rate of 4 points/K.

Thermoelectric Property Measurements. Samples in the form of discs (typically, a 1 mm thick and 12 mm diameter slice) were cut from the cylinder using a diamond saw for electrical- and thermal-transport properties, whereas the Seebeck coefficient measurement was performed on the remaining cylinder.

The electrical resistivity (ρ) was measured using the van der Pauw technique with a current of 100 mA using a special high-temperature apparatus.[23] The Hall coefficient was measured in the same apparatus with a constant magnetic field value of about 10 000 G. The carrier density was calculated from the Hall coefficient R_H, assuming a scattering factor of 1.0 in a single-carrier scheme, by $n = 1/R_H e$, where n is the density of free electrons and e the charge of the electron. The Hall mobility μ_H was calculated from the Hall coefficient and the resistivity values with $\mu_H = R_H/\rho$.

The Seebeck coefficient (S) was measured at room temperature with copper−constantan probes and at high temperature using a high-temperature light pulse technique with Nb/W thermocouples.[24] Nb/W thermocouples have low accuracy below about 400 K, so these data were omitted.

The thermal diffusivity and heat capacity were measured by laser flash technique in a Netzsch LFA 457 system up to 900 °C in a dynamic vacuum using a pyroceram standard for heat-capacity

(16) Saramata, A.; Svensson, G.; Palmqvist, A. E. C.; Stiewe, C.; Mueller, E.; Platzek, D.; Williams, S. G. K.; Rowe, D. M.; Bryan, J. D.; Stucky, G. D. *J. Appl. Phys.* **2006**, *99*, 023708.
(17) Mudryk, Y.; Rogl, P.; Paul, C.; Berger, S.; Bauer, E.; Hilscher, G.; Godart, C.; Noel, H.; Saccone, A.; Ferro, R. *Physica B* **2003**, *328*, 44.
(18) Mudryk, Y.; Rogl, P.; Paul, C.; Berger, S.; Bauer, E.; Hilscher, G.; Godart, C.; Noel, H. *J. Phys.: Condens. Matter* **2002**, *14*, 7991.
(19) Kuznetsov, V. L.; Kuznetsova, L. A.; Kaliazin, A. E.; Rowe, D. M. *18th International Conference on Thermoelectrics*; IEEE: New York, 1999; p 177.
(20) Nataraj, D.; Nagao, J.; Ferhat, M.; Ebinuma, T. *J. Appl. Phys.* **2003**, *93*, 2424.
(21) Nataraj, D.; Nagao, J.; Ferhat, M.; Ebinuma, T.; Anno, H. *21st International Conference on Thermoelectrics*; IEEE: New York, 2002; 72.
(22) Condron, C. L.; Porter, R.; Guo, T.; Kauzlarich, S. M. *Inorg. Chem.* **2005**, *44*, 9185.
(23) McCormack, J. A.; Fleurial, J. P. *Mater. Res. Soc. Symp. Proc.* **1991**, *234*, 135.
(24) Wood, C.; Zoltan, D.; Stapfer, G. *Rev. Sci. Instrum.* **1985**, *56*, 719.

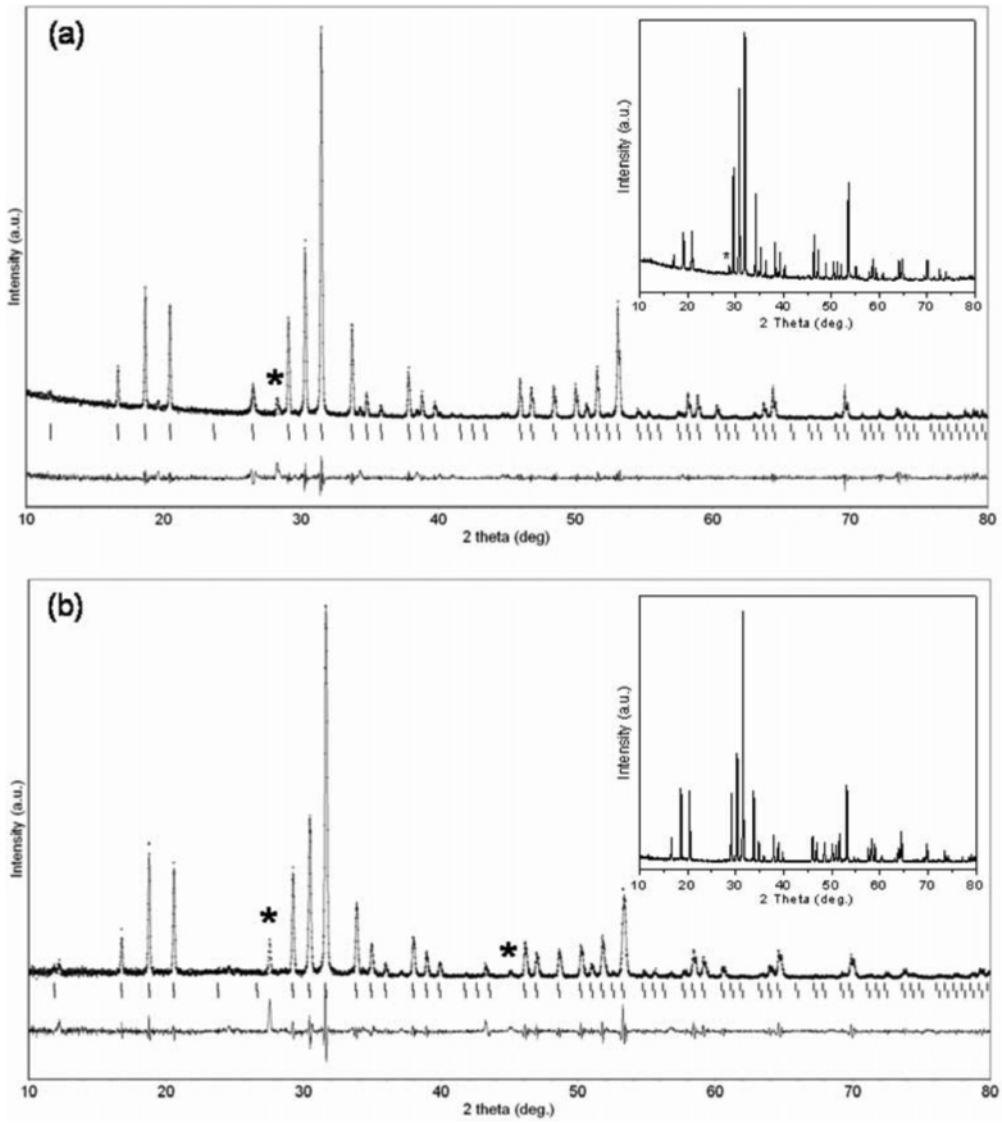

Figure 1. Rietveld profile fit for (a) $Ba_8Al_{14}Si_{31}$, $a = 10.62731(5)$, $R_p = 10.55\%$, $R_{wp} = 15.66\%$, and $\chi^2 = 1.98\%$ (* indicates Si peak); (b) $EuBa_7Al_{13}Si_{33}$, $a = 10.6143(4)$, $R_p = 12.44\%$, $R_{wp} = 19.44\%$, and $\chi^2 = 2.78\%$ (* indicates impurity phase). Experimental data points are shown as black crosses, and the theoretical fit is shown as a gray solid curve. The data were refined for the space group $Pm\bar{3}n$ (black ticks), and the difference between the observed and theoretical patterns is shown below the black ticks. The insets show the X-ray powder patterns before hot-pressing.

measurements. The heat capacity was found to be close to the Dulong−Petit ($3k_b$/atom) value, with a slight linear increase with temperature. A linear fit to the heat capacity and the experimental density was used to calculate the thermal conductivity from the thermal diffusivity measurements.

Results and Discussion

Figure 1 shows the X-ray powder diffraction patterns of (a) $Ba_8Al_{14}Si_{31}$ and (b) $EuBa_7Al_{13}Si_{33}$, respectively, before (inset) and after the samples were hot-pressed. All peaks could be indexed to the clathrate type I structure except for the peak attributed to the most intense reflection of Si in $Ba_8Al_{14}Si_{31}$ and a peak attributed to one of the minority phases in $EuBa_7Al_{13}Si_{33}$, which will be discussed in the next section. The powder pattern of $EuBa_7Al_{13}Si_{33}$ before hot-pressing does not contain the impurity phase peaks. The Rietveld refinement of $Ba_8Al_{14}Si_{31}$ yielded $a = 10.62731(5)$ Å, $R_p = 10.55\%$, $R_{wp} = 15.66\%$, and $\chi^2 = 1.98\%$. Similarly, the Rietveld refinement of $EuBa_7Al_{13}Si_{33}$ yielded $a = 10.6143(4)$ Å, $R_p = 12.44\%$, $R_{wp} = 19.44\%$, and $\chi^2 = 2.78\%$. The lattice parameter for $Ba_8Al_{14}Si_{31}$ is in good agreement with previously published results for the ideal phase, $Ba_8Al_{16}Si_{30}$ (10.6285(4) Å).[18] The lattice parameter for $EuBa_7Al_{13}Si_{33}$ is larger than that reported for $Eu_2Ba_6Al_8Si_{36}$ at 10.496(2) Å.[18] This is expected, however, because of the larger amount of Al in the framework of $EuBa_7Al_{13}Si_{33}$. X-ray diffraction is not sufficiently sensitive to distinguish between Al and Si, because they are very close in electron density. Therefore, refinement of atomic positions and thermal parameters was not performed. Powder X-ray diffraction was used to confirm that these phases were type I clathrate phases and to obtain a unit-cell parameter. For this reason, the residuals are somewhat higher than if full structure analysis were performed; however, the residuals are acceptable for refinement of the lattice parameters.

Because refinement of the X-ray powder diffraction data could not distinguish Al and Si, element analysis from microprobe analysis was used to establish stoichiometry. Figure 2 displays the back-scattered electron image (BSEI) and X-ray maps of Ba, Al, and Si for the polished hot-pressed

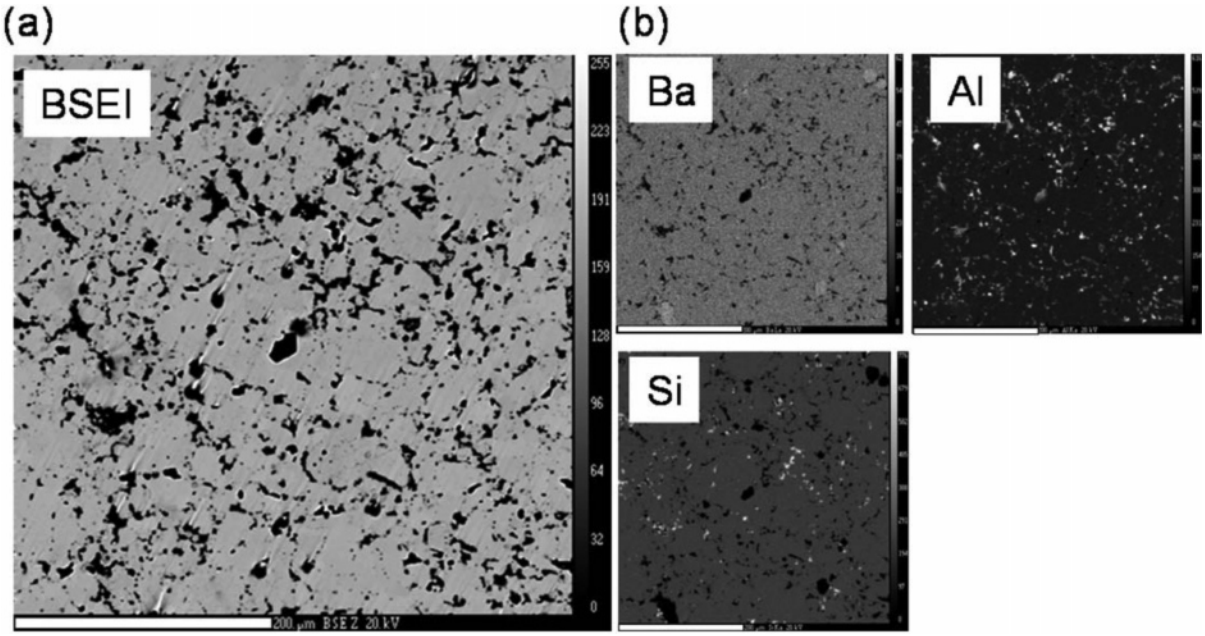

Figure 2. Back-scattered electron image (BSEI) of $Ba_8Al_{14}Si_{31}$, and X-ray maps at 15 kV of Ba, Al, and Si, respectively, for the polished hot-pressed pellet of $Ba_8Al_{14}Si_{31}$. Scale bar is 200 μm for both the BSIE and X-ray maps.

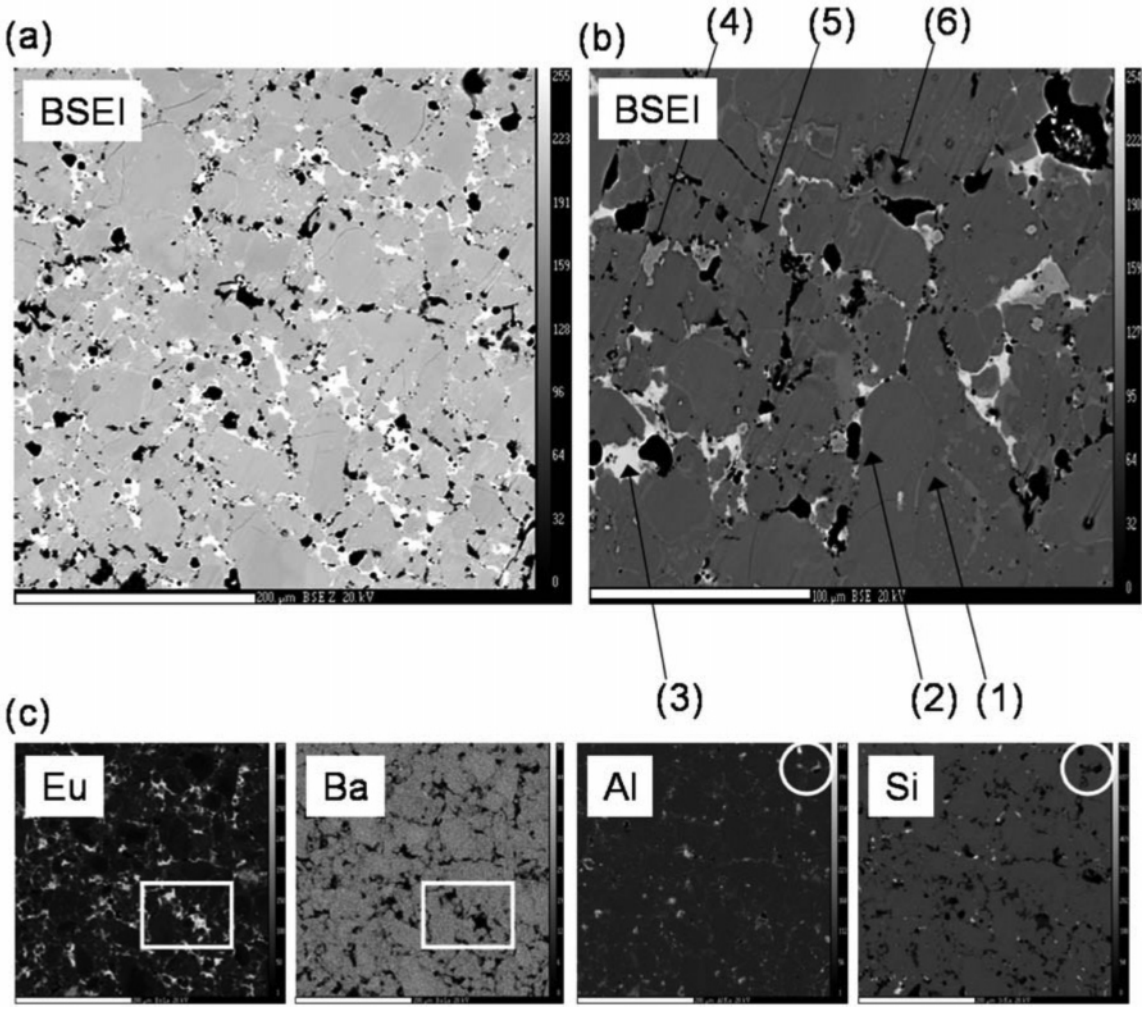

Figure 3. (a) Back-scattered electron image (BSEI) at 200 μm of $EuBa_7Al_{13}Si_{33}$, (b) close up of the BSEI at 100 μm, and (c) X-ray maps at 200 μm and 15 kV of Eu, Ba, Al, and Si, respectively, for the polished hot-pressed pellet of $EuBa_7Al_{13}Si_{33}$. Regions where the stoichiometry was obtained are indicated and also provided in Table 1. The box and circle provide a reference for comparing the same place in the elemental mapping.

pellet of $Ba_8Al_{14}Si_{31}$. Figure 3a−c displays the BSEI, a close up of the BSEI, and X-ray maps of Eu, Ba, Al, and Si, respectively, for polished hot-pressed pellets of $EuBa_7Al_{13}Si_{33}$. The close-up of the BSEI is presented to better see the

Table 1. Average Atomic Percent of Elements (standard deviation in parentheses) for a Hot-Pressed Pellet of $EuBa_7Al_{13}Si_{33}$ (various regions are as indicated in Figure 4)

region	average at % of elements				average stoichiometry
	Eu	Ba	Al	Si	
majority (1)	0.836(0.4)	13.991(0.3)	24.38(0.2)	60.79(0.1)	$Eu_{0.45}Ba_{7.6}Al_{13}Si_{33}$[b]
majority (2)	2.036(0.6)	12.874(0.6)	23.84(0.3)	61.25(0.3)	$Eu_1Ba_7Al_{13}Si_{33}$[a]
Eu-rich (3)	21.15(0.2)	0	37.52(0.1)	41.03(0.2)	$EuSi_2Al_2$[c]
Al-rich (4)	14.08(0.04)	15.25(0.1)	65.16(1.1)	5.51(1.2)	$EuBaAl_{4.6}Si_{0.4}$[c]
minority (5)	5.17(0.5)	9.79(0.6)	23.25(0.3)	61.82(0.3)	$Eu_3Ba_5Al_{12}Si_{33}$[a]
minority (6)	14.8(0.3)	3.245(0.5)	61.82(0.2)	33.75(0.4)	$Eu_7Ba_1Al_{30}Si_6$[a]

[a] Normalized so that Eu + Ba = 8.00. [b] Normalized so that Al + Si = 46.00. [c] Normalized so that Eu = 1.

different regions within the pellet. The X-ray maps for each phase are the same region as that shown in the BSEI (a) for both figures. In the X-ray maps, regions that are brighter indicate a higher concentration of the element being irradiated, and regions that are darker indicate lower concentrations. The very dark regions in the BSEI and X-ray maps are cracks or valleys in the polished pressed pellets. These cracks or valleys can help align the X-ray maps so that the same region in each map can be identified. The BSEI as well as the X-ray maps show that the $Ba_8Al_{14}Si_{31}$ pellet is relatively stoichiometric, whereas $EuBa_7Al_{13}Si_{33}$ pellet is not uniform in stoichiometry, as indicated by the gradation in light and dark regions in the BSEI image. The $Ba_8Al_{14}Si_{31}$ pellet contains the majority phase, $Ba_{8(0.07)}Al_{13.99(0.3)}Si_{30.82(0.2)}$, and a small amount of minority phases $BaAl_2O_4$. Additionally, the very bright regions in the X-ray maps (Figure 2b) for Al and Si show that the sample contains excess Al and Si and is consistent with the X-ray powder pattern for $Ba_8Al_{14}Si_{31}$. This sample will be referred to as $Ba_8Al_{14}Si_{31}$.

The $EuBa_7Al_{13}Si_{33}$ pellet contains several different stoichiometries mostly consistent with type I clathrate stoichiometries. The majority and minority phases are labeled in the BSEI image (Figure 3b) and summarized in Table 1. There are two majority phases that have slightly different stoichiometries: $Eu_{0.45}Ba_{7.6}Al_{13}Si_{33}$ and $EuBa_7Al_{13}Si_{33}$. They are similar in framework composition but different in Eu and Ba content. The Eu-rich region, labeled (3) in Figure 3b, has the highest concentration of Eu and the lowest concentration of Ba. This is clearly observed in the Eu X-ray map (brightest regions) and in the Ba X-ray map (darkest regions). Note that the pattern of each region matches with the corresponding element's X-ray map; a box is outlined to better show the same region in the Eu and Ba X-ray maps. Similarly, the Al region, labeled (4) in Figure 3b, has the highest concentration of Al and the lowest concentration of Si and is also clearly observed in the Al and Si X-ray maps. A circle is indicated in both the Al and Si X-ray maps to better indicate the same region within the maps of the two elements. The empirical formula as determined for the elemental ratios for region 3 and region 4 are $EuAl_2Si_2$ and $BaEuSi_{0.4}Al_{4.6}$, respectively. The two remaining minority phases are clathrate phases and have stoichiometries $Eu_3Ba_5Al_{12}Si_{33}$ and $Eu_7BaAl_{30}Si_{6.4}$ and are present only at the grain boundaries. The small amounts of these impurity phases, along with similar lattice parameters with respect to the majority phases, makes it difficult to discern the inhomogeneity of the sample using X-ray powder diffraction alone. The powder diffraction pattern before the hot-pressing was consistent with clathrate I phase, and impurities became evident after the hot-pressing. This mixture will be referred to hereafter as $EuBa_7Al_{13}Si_{33}$, according to the majority phase.

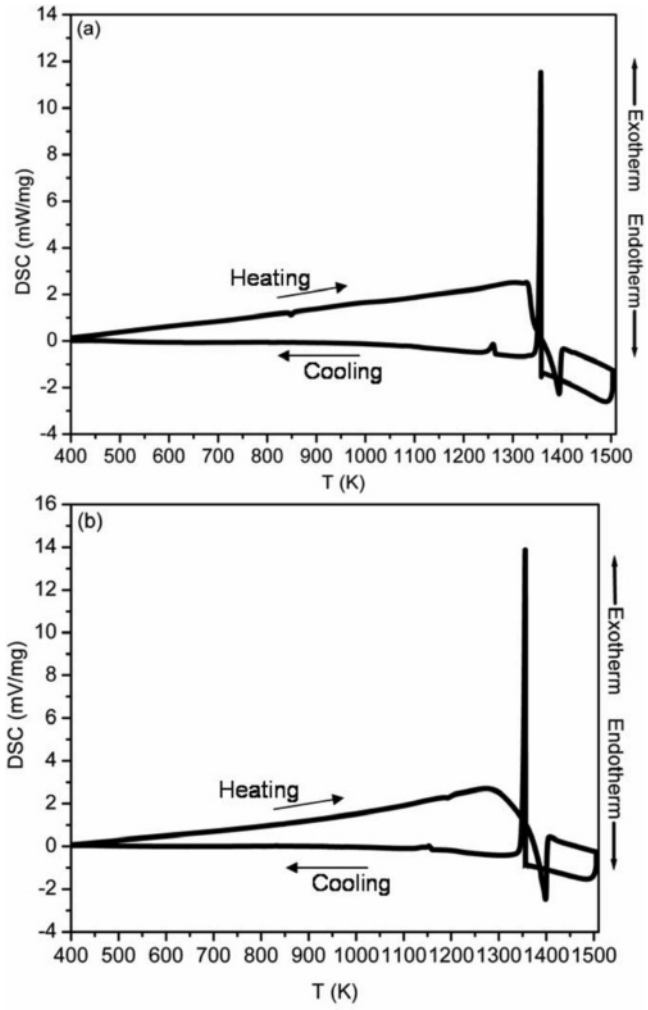

Figure 4. DSC (mV/mg) traces as a function of temperature for (a) $Ba_8Al_{14}Si_{31}$ and (b) $EuBa_7Al_{13}Si_{33}$. Data were obtained by heating/cooling at a rate of 4 K/min under argon. Arrows indicate heating and cooling data.

The DSC scans as a function of temperature for a piece of the hot-pressed pellet of $Ba_8Al_{14}Si_{31}$ and $EuBa_7Al_{13}Si_{33}$ are presented in panels a and b of Figure 4, respectively. In both cases, there is negligible weight loss, or weight gain. The DSC traces versus temperature display a broad endotherm (melting) from 1300 to 1400 K for $Ba_8Al_{14}Si_{30}$ and 1357 to 1400 K for $EuBa_7Al_{13}Si_{33}$ and a sharp exotherm (recrystallization) at 1355 and 1360 K for $Ba_8Al_{14}Si_{31}$ and $EuBa_7Al_{13}Si_{33}$, respectively. There are additional small peaks in both samples that cannot be identified as any impurity phases or any of the elements. The broad melting transition

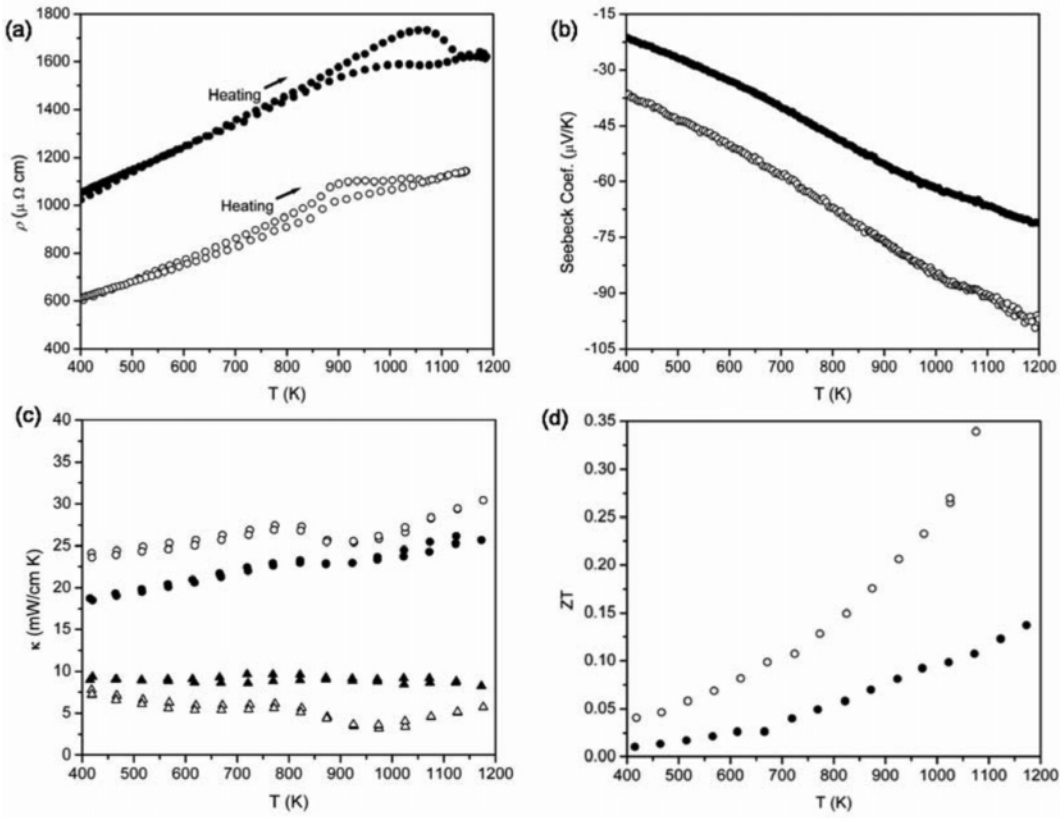

Figure 5. Temperature dependence of the (a) resistivity, (b) Seebeck coefficient, (c) total thermal conductivity (circles) and lattice thermal conductivity (triangles), and (d) zT for $Ba_8Al_{14}Si_{31}$ (open symbols) and $EuBa_7Al_{13}Si_{33}$ (filled symbols) hot-pressed pellets.

Table 2. Room-Temperature Seebeck Coefficient (S), Electrical Resistivity (ρ), Electron Concentration (n), and Hall Mobility (μ_H)

compd	S (μV/K)	ρ (mΩ cm)	n (cm^{-3})	μ_H (cm^2 V^{-1} s^{-1})
$Ba_8Al_{14}Si_{31}$	−35	0.54	1×10^{21}	2
$EuBa_7Al_{13}Si_{33}$	−7	0.94	1×10^{21}	3

and extra peaks in the DSC are attributed to the presence of multiple phases of slightly different stoichiometry and the presence of impurities.

The temperature dependence of the electrical resistivity and Seebeck coefficient are shown in panels a and b of Figure 5, respectively. In Table 2, the room-temperature Seebeck coefficient electrical resistivity and carrier concentration of the clathrate compounds are provided. Both $Ba_8Al_{14}Si_{31}$ and $EuBa_7Al_{13}Si_{33}$ possess n-type conductivity, as indicated from both the Hall effect and thermopower measurements. These values are comparable to those found in $Ba_8Ga_{16}Ge_{30}$ and $Ba_8Ga_{16}Si_{30}$.[19] The electrical resistivity of $Ba_8Al_{14}Si_{31}$ and $EuBa_7Al_{13}Si_{33}$ increase with increasing temperature, characteristic of metallic or heavily doped semiconductor behavior. The absolute value of the Seebeck coefficient gradually increases with increasing temperature and exhibits a maximum of − 99 and −71 μV/K at 1192 K, respectively. Mudryk et al. reported the room-temperature Seebeck coefficient for the phase $Eu_2Ba_6Al_8Si_{36}$ to be −8 μV/K, which is very close to our measured room-temperature Seebeck coefficient for $EuBa_7Al_{13}Si_{33}$.

There are clear differences between the transport properties of the $Ba_8Al_{14}Si_{31}$ sample reported here and the $Ba_8Al_{16}Si_{30}$ sample reported by Mudryk et al.[17,18] Namely, the room-temperature resistivity (0.85 mΩ cm) and the absolute value of the Seebeck coefficient (− 49 μV/K) for $Ba_8Al_{16}Si_{30}$ reported by Mudryk et al. are higher than those of $Ba_8Al_{14}Si_{31}$. This can be attributed to a lower free-carrier concentration in $Ba_8Al_{16}Si_{30}$ due to the difference in chemical composition. Microprobe analysis of the sample reported here yielded a stoichiometry closer to $Ba_8Al_{14}Si_{31}$, whereas the $Ba_8Al_{16}Si_{30}$ phase presented by Mudryk et al. is reported to be on stoichiometry.[17,18] $Ba_8Al_{16}Si_{30}$ has a slightly lower valence electron count per framework atom (or per Al/Si atoms) than $Ba_8Al_{14}Si_{31}$, which can account for the lower carrier concentration. As the sample becomes closer to the valence precise stoichiometry of $Ba_8Al_{16}Si_{30}$, the resistivity and the absolute value of the Seebeck coefficient should increase. A similar effect is also expected from Eu-doped samples, but because of the inhomogeneities, it is difficult to make meaningful structure property correlations.

Differences in electronic-transport properties for the clathrates that are the same nominal stoichiometry but prepared differently are not uncommon and are presumed to be due to small chemical or defect concentrations producing significant differences in free-charge-carrier concentrations. For example, previous reports on Ga−Ge framework clathrates, prepared by different methods, yield different electronic and thermal properties, even though the stoichiometries are reported to be the same.[25,26]

There are two components to the thermal conductivity. The electronic component (κ_e) depends on the electrical

(25) Bryan, J. D.; Blake, N. P.; Metiu, H.; Stucky, G. D.; Iversen, B. B.; Poulsen, R. D.; Bentien, A. *J. Appl. Phys.* **2002**, *92*, 7281.
(26) Nolas, G. S.; Cohn, J. L.; Slack, G. A.; Schujman, S. B. *Appl. Phys. Lett.* **1998**, *73*, 178.

conductivity and can be estimated using the Wiedemann−Franz law, $\kappa_e = L_0T(1/\rho)$, where L_0 is the Lorenz number, ρ is the electrical conductivity, and T is temperature. The free-electron value, $L_0 = 2.44 \times 10^{-8}$ W Ω K^{-2}, was used in calculating the lattice thermal conductivity. The second component is the lattice component and depends on structural details such as structural complexity and disorder. Figure 5c shows the total thermal conductivity, κ, and lattice thermal conductivity, κ_l, for $Ba_8Al_{14}Si_{31}$ and $EuBa_7Al_{13}Si_{33}$. The lattice thermal conductivity is low and consistent with the low lattice thermal conductivities exhibited by most clathrate phases. Taken together, these data for $Ba_8Al_{14}Si_{31}$ provide a zT of 0.34 at 1150 K, and for $EuBa_7Al_{13}Si_{33}$, a zT of 0.22 at 1165 K, as shown in Figure 5d.

The Seebeck coefficient of $EuBa_7Al_{13}Si_{33}$ is lower than that of $Ba_8Al_{14}Si_{31}$, and consequently, the thermal conductivity is expected to be higher than that of $Ba_8Al_{14}Si_{31}$. The lower thermal conductivity of $EuBa_7Al_{13}Si_{33}$ is ascribed to the added disorder caused by impurity scattering. Although there is much published on clathrate phases, little has been published on the microstructure, and therefore, it is difficult to compare implicitly with other phases. These results provide some indication that inhomogeneities and grain boundaries may be important. Impurities at the grain boundaries may not affect the electronic properties because they are extrinsic, but may affect the thermal properties by lowering the thermal conductivity due to impurity scattering, as is the case for $EuBa_7Al_{13}Si_{33}$. In this way, the Seebeck would remain the same and the thermal conductivity would decrease, resulting in an increase in zT. It is possible that composite phases may provide improved thermoelectric properties,[27] and further investigations are necessary to confirm this.

Summary

$Ba_8Al_{14}Si_{31}$ and $EuBa_7Al_{13}Si_{33}$ have been prepared via solid-state reaction of the elements at high temperature. Hot-pressing into pellets provides $Ba_8Al_{14}Si_{31}$ as a single-phase compound and $Eu_1Ba_7Al_{13}Si_{33}$ as a multiphase material. The melting points of both phases are above 1300 K, making them ideal for high-temperature thermoelectric applications. Both samples show heavily doped n-type conductivity. Thermal conductivities are also low, comparable to other clathrate phases. The absolute values of the Seebeck coefficients are not significantly large, but give rise to reasonable zT values for $Ba_8Al_{14}Si_{31}$ at high temperatures. The zT for $Ba_8Al_{14}Si_{31}$ is promising, and optimization of the stoichiometry may provide a low-density material with higher zT. Efforts are underway in this direction.

Acknowledgment. This research was funded by NASA and the NSF, DMR-0600742. The authors gratefully acknowledge Dr. Alexandra Navrotsky for use of the Scintag powder diffractometer and Dr. Sarah Roeske for assistance with microprobe analysis.

CM061483U

(27) Condron C. L.; Kauzlarich, S. M.; Gascoin, F.; Snyder, G. J. *J. Solid State Chem.* **2006**, *179*, 2252.